STUDY OF TEMPERATURE HETEROGENEITIES AT SUB-KILOMETRIC SCALES AND INFLUENCE ON SURFACE-ATMOSPHERE ENERGY INTERACTIONS

Vicente García-Santos[1,2], Joan Cuxart[2], Maria Antonia Jiménez[2], Daniel Martinez-Villagrasa[2], Gemma Simó[2], Rodrigo Picos[2], Vicente Caselles[1]

***Abstract*— The retrieval of land surface temperature (LST) from remote sensing techniques has been studied and validated during the past forty years, leading to important improvements. Accurate LST values are currently obtained through measurements using medium-resolution thermal infrared (TIR) sensors. However, the most recent review reports demonstrated that future TIR LST products need to obtain reliable temperature values at a high spatial resolution (100 m or higher) to study temperature variations between different elements in a heterogeneous kilometric area. The launch of high-resolution TIR sensors in the near future requires studies of the temporal evolution and spatial heterogeneities of the elements in a mixed region. The present study analyzes the LST in a sub-kilometric highly heterogeneous area, combining the use of LST products from high-resolution TIR orbiting sensors with the LST maps created from a TIR camera onboard an unmanned aerial vehicle (UAV). The aim is to estimate the LST variability in a heterogeneous area containing different surfaces (roads, buildings, grass, etc.), observed from different TIR sensors at different spatial resolutions, covering from the meter to the kilometer scales. Several results showed that variations in the LST up to 18 °C were identified with the UAV-TIR camera, and significant differences were also present in the LST products obtained from simultaneous overpasses of high-resolution satellite TIR sensors. A second objective of the study, due to the availability of the high-resolution LST fields, was to explore the thermal advection between the different elements and determine if it correlates with the surface energy budget in the same area, thus indicating that this process is of importance for heterogeneous terrains at these scales. This study also highlights the relevance of the UAV-TIR camera flight for future studies since it is not commonly used in TIR remote sensing but has substantial potential advantages.**

***Index Terms*—Land surface temperature, Remote sensing, Surface heterogeneity, Surface-atmosphere exchange fluxes, Unmanned aerial vehicle, Thermal advection.**

"This work was funded through the projects MINECO/AEI Spanish research projects CGL2012-37416-C04-01, CGL2013-46862-C2-1-P, CGL2015-65627-C3-1-R and CGL2015-64268-R and through a TORRES QUEVEDO Project granted to Vicente García-Santos with reference PTQ-16-08578, of the Spanish Government, supplied by the European Regional Development Fund (FEDER), and the project PROMETEOII/2014/086 of the Government of Generalitat Valenciana. This study was also supported by the pre-doctoral contract of Mrs. Gemma Simó (BES-2013-065290) financed by the Spanish Government."

1. Department of Earth Physics and Thermodynamics, Faculty of Physics, University of Valencia, 46100 Valencia, Spain.

2. Department of Physics, University of Balearic Islands, 07122, Palma, Spain.

Corresponding author: vicente.garcia-santos@uv.es

I. INTRODUCTION

LAND surface temperature (LST), recognized as one of the most important Earth System Data Records according to NASA [1], requires accurate estimations with small uncertainty and bias [2]. LST is an important variable that controls processes in several disciplines, such as agro-meteorology [3] or surface-atmosphere interactions [4]. However, recent review reports have stated that in addition to the accurate retrievals of LST, the future of thermal infrared (TIR) remote sensing should use LST products at high spatial resolutions (above 100 m) to obtain reliable temperature values from the different elements composing a heterogeneous kilometric area, considering that the temperature of such elements is more important than the area average value [5]. In previous works [19], it has been proposed that the standard deviation of LST values over a heterogeneous area could be used as a parameter to show the variability in LST. In any case, the LST products from medium resolution TIR sensors (~ 1 km^2) are very reliable and accurate (± 1 °C), as shown by the comparisons with sampling field data measured in highly homogeneous surfaces [6-7]. However, it has been demonstrated that such kilometric LST products are not representative of the temperature of different elements on heterogeneous surfaces [8, 65].

Recent studies indicate the necessity of obtaining LST maps from satellite TIR sensors at a high spatial resolution (60-100 m) to carry out work on heterogeneous zones, such as the monitoring of the urban heat island effect and control of maximum temperatures in cities [9-10], the classification of different surface types to improve irrigation practices [11], the determination of patterns in the temporal evolution of the LST

[12, 70], the management of strategies for forest recovery and reforestation after a fire based on the high sensitivity of the LST to different severity levels of the burned zones [13], the estimation of evapotranspiration (ET) maps at spatial resolutions lower than 100 m [14] or the study of the impact of these LST high-resolution maps on the surface fluxes [15].

LST maps at fine scales (below 10 m) have been recently used in some studies by means of TIR cameras mounted in airborne systems, such as helicopters or airplanes, to perform detailed studies of LST heterogeneities associated with small-scale components present in a hectometer area [16]. These studies corroborated that LST products at such finer scales could be useful to retrieve accurate LST values of the leaf in a crop [16, 71], which allows good episodic or seasonal estimations of the ET for this crop [14].

Unmanned aerial vehicles (UAV) are able to determine LST and atmospheric variables. They can make several daily flights. The actual surface that is sampled depends on the vehicle and the legislation that usually limits operation to visual control of the drone by the ground-based operator to a radius of a few hundred meters. The speed of the UAV is usually lower than manned aircraft and allows a higher spatial resolution, discriminating the variations in LSTs at very fine scales. The use of UAVs in remote sensing applications has increased significantly in the last triennium [17]. These applications include a variety of disciplines, such as agriculture, forestry or geology (an interesting list of published studies can be consulted in Table I of [18]).

However, there are very few works about the use of TIR sensors installed in a UAV, and there is room to explore in depth the possibilities of such technology in the TIR remote sensing field. Some of these studies were motivated, for instance, to estimate the importance of the thermal advection at different scales [19], to evaluate the thermal impact of a river on the surrounding agricultural terrain [20] or to compare turbulent energy flux estimates with two surface energy balance (SEB) models based on UAV TIR imagery with high spatial and temporal resolutions [21]. Other types of applications include the accurate mapping of the geothermal heat signature of a geothermal field [22] and monitoring animal populations for conservation purposes [23]. A review of forestry applications of UAVs in Europe with thermal cameras can also be found in the literature [24].

Having access to the variability of LSTs allows the estimation of thermal advection between distinct surface elements of the study area. The surface energy budget considers all the energy exchanges that take place in the atmosphere-surface interface. In this framework, the four main terms (i.e., the net radiation (Rn), turbulent sensible (H) and latent (LE) heat fluxes and the soil (G) heat flux) would be balanced if they are observed over a homogeneous surface (and thus with no thermal advection) and if there are no other thermal sources or sinks. In contrast, with LST heterogeneities, the thermal advection may become important, and the traditional 4-term energy budget would not close. It has been [25] shown that, using two years of data over heterogeneous surfaces, the imbalance of the surface energy budget was usually between 10 to 30% of the R_n, often being the second or third term in importance and overpassing the ground or turbulent heat fluxes, especially at night. These values are in accordance with those provided in the review of [26]. The authors indicated that there were a number of sources to explain the imbalance, including instrumental disposition, lack of stationarity, or missing processes such as biological or anthropic activity or thermal advection. A first estimation of the importance of the advection term was given in [19] using model, satellite and UAV TIR data, where they showed that hectometer scales were likely to contribute significantly to the SEB imbalance if there were persistent heterogeneities present.

A recent study conducted in the Campus of the University of the Balearic Islands (UIB) has shown that the different elements composing this area form a temperature field with large heterogeneities [27]. In that work, the MODIS values for the pixel covering the campus are compared to ground measurements and indicate a larger bias and RMSE values than for similar studies in homogeneous terrain. Furthermore, an analysis of the Landsat and ASTER images indicate large surface variability in LSTs in the range of 10 to 20 °C depending on the season. Such an analysis has been key to plan the current work and a companion study by [28]. In the current case, the main objective is to study the surface temperatures at sub-kilometric scales through a combined inspection of satellite-derived LST products and observations from an UAV. In addition, these fields are used to explore the contribution of such heterogeneities in the imbalance of the SEB.

The paper proceeds as follows: Section II describes the heterogeneous site, the materials and the methods selected for the study. In Section III, the LST products observed from different platforms are presented and validated, while the corresponding heterogeneity results are discussed. An application study estimating the importance of the thermal advection with the SEB equation is demonstrated in Section IV. Finally, conclusions are provided in Section V.

II. Study site and Materials

A. UIB Campus

The study site is located in the campus of the University of the Balearic Islands (UIB), at a height of 80 m above sea level (a.s.l.) in the Palma Basin at Mallorca Island (Figure 1), in the western Mediterranean Sea and 200 km east from the Iberian Peninsula. The UIB campus has an approximate area of 1 km x 1 km, halfway between the city of Palma and the natural area of the Tramuntana Mountain range. It is composed of many different types of surfaces such as buildings, asphalted roads, farming areas, some sloping terrain, fields of orange and almond trees, lawns and some natural vegetation extensions. The natural vegetation includes wild grass between October and May that dies in the summertime, with the surface becoming a mixture of bare soil and dead vegetation.

Recent studies showed the heterogeneity of the UIB Campus in terms of LST with gradients between different surfaces of up to 10 °C in wintertime and up to 20 °C in summertime, during the daytime [27]. During weak large-scale pressure gradients and clear-sky conditions, locally generated winds are present in Mallorca and especially in its three main basins [29-30]. This scenario is the case for the diurnal sea breeze (especially from April to October) or the nocturnal land breeze, both often coupled with slope winds [31].

A complete surface energy budget (SEB) station has been running at the UIB Campus since 2015 (yellow dot in Figure 1). Several data taken for the entire year of 2016 from this station are used in the present study. First, observations from a broadband thermal infrared radiometer (IR120, Campbell Scientific) were taken as a ground reference value to validate several LST products (see Section III). Second, the measured terms of the SEB together with the wind observations are used in Section IV. These contributions to the SEB are the turbulent sensible and latent heat fluxes, the net radiation and the ground heat flux. Turbulent fluxes were measured with a sonic anemometer (81000, RM Young) and a gas analyzer (EC150, Campbell Scientific) after applying the Eddy correlation technique [32]. The net radiation was extracted from the upward and downward components of the solar and longwave radiation observed from the Hukseflux NR01 net radiometer. Finally, the ground heat flux was determined as the contribution of the measured flux by the Hukseflux HFP01 sensor at a certain depth within the soil plus the change in heat storage in the soil above the plate [33], which was estimated using soil temperature and water content measurements [34]. The IR120 radiometer operates in the 8-14 μm spectral range and has an FOV of 36°. This sensor is located at a 1-m height, measuring the LST representative of a circumference with 2 m of diameter.

In situ LST (in °C) is calculated from the measured upwelling longwave radiance ($L^{\uparrow}$, in Wm^{-2}) as:

$$\mathrm{LST} = \left[\frac{L^{\uparrow} - (1-\varepsilon)L^{\downarrow}}{\varepsilon\sigma}\right]^{1/4} \quad (1)$$

where $\varepsilon = 0.97$ is the selected value for the broadband emissivity surface [35], corresponding to senescent sparse shrubs and $\sigma = 5.67 \cdot 10^{-8}$ $Wm^{-2}K^{-4}$ represents the Stefan–Boltzmann constant. Reflected downwelling radiance ($L^{\downarrow}$, also in Wm^{-2}) is calculated from the Brutsaert approximation [36], as it is done in [28].

Ground-based LST observations correspond to the 1-min average measurements. The IR-120 radiometer was calibrated in the laboratory against the reference blackbody model LANDCAL P80P. In 2009, the P80P blackbody participated in a comparison campaign organized by the Committee on Earth Observation Satellites in the National Physical Laboratory (NPL). The results showed that the P80P blackbody agreed with the NPL reference radiometer within ±0.15 °C at 20 –30 °C [37]. The reference blackbody temperature ranged within 0-60 °C, showing an RMSE on the retrieved LST from the IR -120 radiometer data of ± 0.4 °C.

B. MODIS data

The Moderate Resolution Imaging Spectroradiometer (MODIS) onboard the Terra and Aqua satellites currently provides global coverage, twice-daily LST, and emissivity products generated from two different algorithms: MOD11_L2 (MYD11_L2 for Aqua) and MOD11B1 (MYD11B1 for Aqua). The MOD11_L2 product uses the generalized split-window algorithm [38] and provides LSTs and classification-based emissivities for bands 31 (10.8–11.3 μm) and 32 (11.8–12.3 μm) at 1-km resolution. In this study, the LST product used was the MOD11_L2 with refinements proposed in its version 6 [39]. Two images (day and night) of the MOD11_L2 LST product were downloaded from the NASA webpage (https://reverb.echo.nasa.gov) for July 21st, 2016. These scenes were acquired in cloudless conditions, and the associated LST uncertainty included in the product stipulates a value of 1 °C. This uncertainty is only an estimated value, but it is quite conservative in real clear-sky conditions [39].

C. ASTER data

The Advanced Spaceborne Thermal Emission and Reflection Radiometer (ASTER, [40]) is also a MODIS onboard the sun-synchronous Terra satellite. The ASTER uses five TIR bands to measure the Earth's emittance within the 8-13 μm range, offering an LST and emissivity (ε) product at 90 m x 90 m spatial resolutions every 16 days but with an 8% duty cycle, after applying the semi-empirical temperature and emissivity separation (TES, [41]) method. The uncertainties associated with LST and ε after the TES method are 1.5 °C and 0.015, respectively. The retrieval of the ASTER LST from the TES shows inaccurate estimates over surfaces with low emissivity spectral contrast or under humid atmospheric conditions [42]. To minimize the LST errors associated with atmospheric correction, [43] proposed a water vapor scaling (WVS) method that improves the accuracy of the water vapor atmospheric profiles on a band-by-band basis for each observation. Implementing both the WVS and TES methods showed a significant improvement in the retrieved LST [44, 6].

ASTER-Terra overpasses the UIB Campus twice a day, every 16 days, approximately 1049 UTC (morning scene) and 2153 UTC (night scene). A total of 11 (6 at morning, 5 at night) cloudless ASTER images were acquired between April and November 2016 over the UIB Campus. Table I shows the date and UTC hour of the cloudless ASTER scenes used in this study. ASTER image acquisition is an on-demand service, so we requested collection images over our Mallorca site.

D. Landsat 7- ETM+ data

The Enhanced Thematic Mapper Plus (ETM+) onboard the heliosynchronous Landsat 7 covers the entire Earth in 16 days. The ETM+ measures the radiance in eight spectral bands ranging from the visible spectrum to the TIR range with a spatial resolution of 30 m x 30 m. The TIR band 6 (10-12 μm) is disaggregated from 60 m to 30 m by the Landsat team [45]. A failure in the scan line corrector (SLC-off mode) occurred in 2003, and since then, the ETM+ images have been affected by a 100-m strip line of void-data, every kilometer. The location of Mallorca Island allows an increase of the overpass frequency of the Landsat 7-ETM+ to every 7–9 days, at approximately 1030 UTC because the island is placed between the pass of two different orbits of Landsat 7-ETM+, which scan the island from the north (path/row 197/32) and the south (path/row 196/33). Figure 2 shows an RGB view of both Landsat 7-ETM+ overpasses over Mallorca Island.

The retrieval of the LST from Landsat 7-ETM+ is based on the single-channel method [46], which applies atmospheric and surface corrections to the top of atmosphere (TOA) spectral ETM+ radiance ($L_{TOA,i}$, in $Wsr^{-1}m^{-2}\mu m^{-1}$) measurements at band 6. The LST is cleared from the radiative transfer equation (RTE) in (2):

$$L_{TOA,i} = \left[\varepsilon_i B_i(\mathrm{LST}) - (1-\varepsilon_i)L^{\downarrow}_{hem,i}\right]\tau_i + L^{\uparrow}_{atm,i} \quad (2)$$

where ε_i is the surface emissivity; B_i(LST) is the Planck function of a blackbody emitting at the surface temperature (LST); and $L^{\downarrow}_{hem,i}$, τ_i and $L^{\uparrow}_{atm,i}$ are the atmospheric parameters corresponding to hemispherical downwelling radiance, atmosphere transmissivity and upwelling radiance, respectively. The subscript i refers to the channel-effective quantity of each parameter in the RTE.

The surface emissivity used in Equation (2) was extracted from the ASTER Global Emissivity Database (GED) [47]. The ASTER-GED offers surface emissivity values at a 100-m spatial resolution for the five TIR channels of the ASTER sensor based on planetary ASTER TES results data from 2000 to 2008. In this study, the emissivity used to correct the surface emission at the disaggregated TIR image of the ETM+ sensor at 30 m × 30 m pixels was calculated from the weighted averaging ASTER GED values in channels 13 (10.25–10.95 µm) and 14 (10.95–11.65 µm) to the ETM+ TIR band 6, since both channels cover the spectral resolution of such a band. After the convolution process, the 100 m x 100 m resolution data were downscaled to 30 m x 30 m. The emissivity of different components of the UIB Campus ranges between 0.960–0.982, with an average value of 0.972 and a deviation of 0.004. According to [41], the associated emissivity uncertainty is approximately 0.015, and therefore, the LST values might also have an uncertainty of approximately 1.5 °C.

The atmospheric variables $L^{\downarrow}_{hem,i}$, τ_i and $L^{\uparrow}_{atm,i}$ in (2) were calculated with the MODerate resolution atmospheric TRANsmission (MODTRAN) radiative transfer code (v. 5.2.1, [48]) using the synthetic atmospheric profile provided by a web-tool calculator [49] based on the National Centers for Environmental Prediction (NCEP) model [50]. Compared with sounding data, this NCEP profile was demonstrated to be the best option to retrieve atmospheric variables, with respect to other synthetic atmospheric profiles [51]. To retrieve a more accurate synthetic atmospheric profile, the web-tool calculator allows establishing surface conditions of the selected location. These surface parameters consist of the altitude (km), pressure (mb), air temperature (°C) and relative humidity (%), and they were provided in this study at the corresponding UTC time by the SEB station (see section II.A and Figure 1).

Once the variable B_i(LST) was estimated in the RTE from the surface emissivity and atmospheric effects, the LST could be obtained following the expression proposed by [45], with a noise equivalent change in temperature (NEΔT) at 280 K of 0.22 K, as:

$$\mathrm{LST} = \frac{1282.71}{\ln\left(\frac{666.09}{B_i}+1\right)} \quad (3)$$

A total of 19 Landsat 7-ETM+ clear-sky scenes (8 for the 196/33 and 11 for the 197/32 path/row overpass) of the UIB Campus site were used in this study along the year 2016 (see Table II).

E. UAV-TIR camera data

A TIR camera was assembled in a UAV (Figure 3a) to reproduce an LST map of the UIB Campus, at high spatial resolution (2 m x 2 m) flying at a height of 200 m. The TIR camera model is the FLIR LEPTON® Long Wave Infrared [52]. Its dimensions are 11 x 12 x 6 mm and the FOV is 51° and 63.5° in the horizontal and diagonal views, which produces a TIR scene at different spatial resolutions depending on the height of the fly, due to the 80 (horizontal) x 60 (vertical) active pixels in each camera shot, respectively. This TIR camera measures the 6-15 µm integrated value of the spectral radiance of a target. Figure 3b shows the spectral response of the FLIR LEPTON TIR camera between 6-15 µm.

The TIR scene acquisition process consisted of flying the UAV-TIR camera system at a height of 200 m from the red cross in Figure 1 to the north (900 m distance), then turning west (70 m distance), from north to south (900 m distance), and then repeating the entire south-north-west-south process several times to cover the entire campus. The overall process took 20 minutes, including a mid-flight stop to change the battery. The TIR camera took an average of 750 scenes of the whole UIB Campus (a scene every flying second). Table III shows the different UAV flights carried out in the five intensive operative periods (IOPs) programmed in June and July of 2016. It was initially proposed to fly the UAV-TIR camera every 2 hours each IOP day, starting at 0400 UTC and finishing at 2000 UTC. However, due to the battery or UAV system problems, the plan could not be fulfilled completely.

An LST map of each TIR scene was obtained after converting the digital numbers (DN) measured by the FLIR camera into radiance (LFLIR) according to the manufacturer's indications. The LFLIR is a composition of different radiance terms, as in Equation (2). The atmospheric terms were obtained from introducing the NCEP synthetic profile [49], limited between geopotential heights of 0.08 km (altitude of UIB campus) and 0.28 km (height a.s.l. of UAV flight), into the MODTRAN code. The broadband emissivity was considered as a unique constant value of 0.964 ± 0.015, for all pixels of the UIB Campus. It must be taken into account that such emissivity is different from the 0.972 selected for the Landsat 7 ETM+ sensor (see section II.D) because the operational spectral range of both sensors are different. The five different ε_j (j=ASTER channels 10-14) values of the ASTER GED, up-scaled at 1-km^2 resolution [47], were used to retrieve a constant value according to the broadband emissivity expression proposed by [53]:

$$\varepsilon_{UAV} = 0.197 + 0.025\varepsilon_{10} + 0.057\varepsilon_{11} + 0.237\varepsilon_{12} + 0.333\varepsilon_{13} + 0.146\varepsilon_{14} \quad (4)$$

Average emissivity values and the corresponding error are in good agreement with the emissivity range observed in the UIB Campus for the Landsat 7- ETM+ data (see subsection II.D). No directional effects on emissivity [66-68] were considered in this study. Once every single TIR scene was converted to the LST map, they were composed as an overall LST map of the UIB Campus with the privative software Agisoft PhotoScan®.

The FLIR LEPTON TIR camera was also calibrated in the laboratory against the reference LANDCAL P80P blackbody (see section II.A), showing an RMSE on the retrieved TIR camera data of ±2 °C. According to [49], associated errors to synthetic atmospheric profiles are ±2 °C in air temperature and ± 2 % in relative humidity. These uncertainties applied to the atmospheric profiles used in this study and induced a corresponding average uncertainty in the atmospheric parameters $L^{\downarrow}_{hem,i}$, $L^{\uparrow}_{atm,i}$ and τ_i of ±0.06 $Wm^{-2}sr^{-1}\mu m^{-1}$, ±0.09 $Wm^{-2}sr^{-1}\mu m^{-1}$ and ±0.005, respectively. These uncertainties, together with the emissivity error of ±0.015 and TIR camera temperature calibration uncertainty previously mentioned, established a total uncertainty on the LST retrieved from the UAV-TIR camera of ±3 °C. However, the uncontrolled environmental conditions of the camera sensor can consequently lead to uncertainties in the camera performance and in the final LST retrieval.

III. LST HETEROGENEITIES AT SUB-KILOMETRIC SCALE

A. Local validation of LST scenes

The vegetated surface targeted by the IR-120 radiometer is representative of the surface surrounding the SEB station, and it is even representative of the 42% of the surface of the UIB Campus. Therefore, we considered that this LST could be used as a reference to validate the LST product calculated by the ASTER-Terra, Landsat 7-ETM+ and UAV-TIR Camera sensors.

Figure 4 shows the validation results for the LST product of ASTER, ETM+ and TIR Camera compared with the IR-120 radiometer of the UIB budget energy station for all the data obtained for the corresponding sensor in Tables I, III and IV. A comparison between the MODIS LST product and that measured by the ground radiometer was not considered because the spotted surface measured with the IR-120 is not comparable with the kilometric LST value derived by MODIS, especially in a heterogeneous terrain [27]. The ASTER, ETM+ and TIR Camera LST product shows a RMSD with respect to the radiometer temperature of ±1.3 °C, ±1.8 °C and ±3.1 °C, respectively, and a bias of -0.5 °C, -0.5 °C and -0.6 °C, respectively. In the case of the ASTER sensor, an RMSD of ±1.4 °C for both morning and night overpasses was observed. For the ETM+ LST product, RMSDs of ±1.6 °C and ±2.3 °C were observed for the 197/32 and 196/33 path/row orbits, respectively.

The validation results of this study are consistent with previous validation studies. Thus, for the ASTER sensor, LST uncertainties of ±1-2 °C were observed [54-56]. In the case of the Landsat 7-ETM+, the validation results of this study were also in good agreement with a previous UIB Campus study [27] and with other past published works [57-58] where an RMSD of ±1-2 °C was found in the LST product derived from the band 6 of the ETM+ sensor. The RMSD of the UAV-TIR Camera LST product was the expected uncertainty according to the sensitivity study described in section II.E. However, it is worth noting that the TIR camera validation was only accurate for the grass surface (case of SEB station) since in this case, it was well-known that the soil emissivity LST maps of Figure 5 are severely affected by different surface emissivity values. Other sources of error influencing the final uncertainty of these LST products could be the differences in the type of TIR sensor or the heterogeneity of the surfaces present in the UIB Campus.

B. Daily LST heterogeneity of the UIB campus

Once the retrieval methods of the LST product for the 4 different sensors considered (MODIS, ASTER, ETM+ and TIR Camera) have been described and the corresponding uncertainties of such products stipulated, the LST heterogeneity of the UIB Campus was assessed. As commented previously, some of the surface elements of the UIB Campus are assigned an inaccurate emissivity value of 0.964 (see section II.E). For instance, the rooves of the buildings are made with different kind of tiles, which can have emissivity values ranging between 0.93-0.96, or asphalt from roads, which can be assigned an emissivity value of 0.93. This scenario means that some of the LST values obtained from the TIR camera can be inaccurate by several Celsius degrees, and their true values are most likely higher than those estimated in such LST maps. Nevertheless, considering an emissivity value of 0.96, instead of 0.93, may underestimate the LST by approximately 2-3 K, much less than the LST difference considered in this study. Notably, these types of surfaces have a representative extension in the southern region of the UIB Campus, but they do not have an important impact on the advection study carried out in the SEB station since at high resolution within 10-80 m, the surrounding surface is grass and trees, and those have emissivity values close to the selected 0.964 value. In addition, for the lower resolution 90-200 m, the effective emissivity of such buildings is close to the selected emissivity value, according to data extracted from the ASTER GED [47].

However, to avoid an underestimation of the LST value due to an incorrect selection of the emissivity, it is observed that for the four cloudless IOPs and for the central hours of the day (0800-1800 UTC), the hottest point is located at the artificial grass of the soccer field, and the coolest point is usually located in a humid creek area, situated north of the UIB Campus. Both sites have an extension area greater or at the same scale order of 100 x 100 m^2, and according to the emissivity data from the ASTER 100 m GED database and following

Equation (4), the broadband emissivities of the soccer field and the humid creek area are 0.966 and 0.968, respectively. Those emissivities are close to the emissivity selected in section II.E for the whole UIB Campus, so we focused the LST heterogeneity study during the central hours of the day on those two sites for reliable conclusions. However, there could be a cavity effect for the artificial grass of the soccer field, which would cause the humid creek to appear colder than the soccer field.

Figure 5 shows the LST maps of the UIB Campus for four of the nine UAV-TIR camera flights (0400, 1000, 1200 and 2200, UTC) during IOP5 (21/07/2016). The registration problems (maps a, b, c and d do not stack) in these LST maps are due to the limitation of the privative software when assembling the TIR images taken by the UAV-TIR camera. The LST variability shown in maps of Figure 5 is representative of the four IOPs carried out in cloudless conditions (IOP 1, 2, 3 and 5). These IOPs showed significant LST differences within the campus from the first flight. The maximal LST variations observed in each IOP ranged within 3-28 °C during the day. They ranged 3-10 °C during the two first flights before the sunrise (0400-0600 UTC). The LST differences between the soccer field (warm point) and humid creek area (cold point) reached significant values of 6-28 °C during the central hours of the day (0800-1600 UTC). The last three flights before the sunset (1800-2200 UTC) showed a slightly decreased LST variability of 6-12 °C. The LST difference at the early hours of the morning (0400-0600 UTC) and later hours close to sunset (1800-2200 UTC) are usually attributed to the difference between the LSTs of roads (hot point) and rooves of some buildings (cold point). It is worth mentioning again that these differences could be reduced by several Celsius degrees since an inaccurate emissivity value was assigned to these types of surfaces.

The IOP 4 (14/07/2016) and the early hours of the IOP 5 were the only cases with an overcast sky and showed that the LST variability in the majority of the flights that day remained stable, ranging within 3-5 °C (see later Figure 8). Therefore, under the same radiant lighting conditions, the LST variability of the heterogeneous surfaces in the UIB Campus seemed to be less significant but still needs to be taken into account. The IOP 4 showed the important advantage of using the UAV since under cloudy conditions, there was no possibility of retrieving the LST products from the TIR satellite sensors.

C. LST heterogeneity from orbiting sensors

The simultaneous overpass of the three TIR sensors mentioned (MODIS, ASTER and ETM+) matched with a UAV-TIR camera flight in two occasions during the studied period: approximately 1030 UTC of the 05/07/2016 (IOP3) and 21/07/2016 (IOP5).

Figure 6 shows the LST product of the four sensors at their different spatial resolution for the IOP 5 (the shown area is the same shown in Figure 5, so the coordinates are removed). The high LST heterogeneity observed by the UAV-TIR camera product at a resolution of 2 m x 2 m (Figure 6d) was considerably reduced as seen by the spatial resolution of 30 m x 30 m of the LST product calculated for the Landsat 7-ETM+ TIR data (Figure 6c), where almost all the cold pixels of the UAV LST map were effectively converted to temperate LST values as a consequence of the spatial degradation. The loss of information of the LST heterogeneities was more evident with the LST product offered by the ASTER sensor (Figure 6b) at 90 m x 90 m, and this heterogeneity was imperceptible with the MOD11 LST product (Figure 6a) at 1 km x 1 km.

Despite the loss of the LST information, with the high-resolution LST product of the ETM+ and ASTER sensors with regard to that offered by the UAV-TIR Camera, both sensors still showed significant LST variability. For instance, the maximum LST difference observed between the soccer field and the wet creek in the north of the UIB Campus is 16 °C for the UAV-TIR Camera product; however, the difference was reduced to 11 °C with the ETM+ and to 9 °C with the ASTER LST products, and both differences are still very significant.

Figure 7 shows the LST product offered by the night overpass of the sensors ASTER and MODIS, onboard the Terra platform, compared with the LST product calculated from the simultaneous UAV-TIR camera flight over the UIB Campus. Under those stably stratified thermal conditions at night, significant LST differences were seen, such as the 14 °C value between the artificial grass of the soccer field (cold point) and the road in the southwestern part of the UIB Campus (warm point). This difference was reduced to 7 °C with the LST product offered by the ASTER sensor, which is still very significant. The MODIS showed LST differences of 2 °C for the four pixels covering partially the UIB campus.

Figures 6 and 7 are a clear example that a high spatial resolution on LST products is of key importance to study heterogeneities in zones composed of different surface types. In both cases, it was observed that the pixels composed by dense vegetation, such as the wet creek, showed the coldest zones, and other pixels composed by tarmac roads, bare soil or the soccer field, made with artificial grass, showed the hottest points of the LST map at midday. At midnight, the presence of grass (even the artificial one of the soccer field) and the tiled roof of some buildings were the coldest points, and the influence of tarmac roads produced the hottest pixels of the map. These temperature differences in both cases remained in the LST product of the ETM+ and ASTER sensors, but the MODIS did not show them, since they corresponded to sub-kilometric spatial resolutions.

D. Analysis of the variability of the LST fields over the UIB Campus

To further explore the temporal and spatial variability of the LST fields estimated from the UAV-TIR Camera, ETM+ and ASTER, the corresponding probability density functions (PDFs) were computed over the UIB Campus for all the studied IOPs. As it was described in [59], the shape of the PDF of any magnitude depends on the variability of its values that, together with the statistics computed from it, allows estimating the heterogeneity of the field [60]. Figure 8 shows the PDFs computed from the LST fields from the UAV-TIR Camera, ETM+ and ASTER over the UIB-Campus for all IOPs at different instants to cover the diurnal cycle. The temporal evolution of the statistics is shown in Figure 9 to check if the variability of the LST fields is similar for all IOPs through the inspection of the standard deviation (σ, gives information about the spread of the LST values within the UIB Campus) and the skewness (S, points out the prevalence of values larger or smaller than the mean one, corresponding to negative and positive S values, respectively).

Figures 8 and 9 indicate that the analysis of the PDFs is a useful tool to compare the spatial and temporal variability of the different sources of the LST (as those shown in Figures 6 and 7 as an example of a day and night instant, respectively) used in this work for the studied IOPs. It was found that the diurnal cycle of the variability of the LST fields reported by the UAV-TIR camera was similar for all IOPs (similar shapes in the PDFs in Figure 8 and very close values of σ and S in Figure 9). However, IOP 4 presented a distinct behavior with statistics close to normal values (small σ and S close to 0). The presence of clouds during this IOP reduced the variability of the LST field and was probably linked to a decrease in the net radiation at the surface that did not allow the growth of the thermal heterogeneities due to the different surface properties. A similar pattern was also found for IOP 1 at 0400 UTC (Figure 8a), when the PDF was narrower than the others due to the presence of clouds during the late night and early morning that disappeared as the day advanced, resulting in similar PDF shapes as IOPs 2, 3 and 5 (for instance, at 1200 UTC, Figure 8c).

During the central hours of the day for clear-sky IOPs, the standard deviation reached the largest values of the diurnal cycle (Figure 9a) in agreement with the results of another study carried out in the UIB Campus [27]. In addition, the PDFs were biased with negative skewness demonstrating that the most frequent values are those LST values were warmer than that of the mean. As a result, the analysis of all IOPs showed that heterogeneities were largest during the day, and they were linked to the different surface properties of the ground within the UIB Campus (Figure 5). During the morning and evening transitions, σ(LST) took the minimal values of the day (minimum in the temporal evolution of σ, Figure 9a) but with a predominance of points with the LST colder than that of the mean (positive S, Figure 9b), demonstrating that most of the surface covers at the UIB Campus had a fast response when the net radiation was close to zero. Finally, during the nighttime, the variability of the LST was larger than during the transitions but was lower than during the day with the equilibrium of the colder and warmer points (S close to zero).

The analysis of the PDFs also demonstrated that the spatial variability of the satellite-derived LST fields (ASTER and ETM+) was smaller than the one reported from the UAV LST fields during day and night (see instants in Tables I, II and III). The spatial resolution of the different sources of LST might be the main reason for such differences in the spatial variability of the LST fields, especially in a heterogeneous area as the UIB Campus studied here. Nevertheless, the spatial variabilities of the satellite LST fields for any of the studied IOP were similar to the one reported by the UAV-TIR camera for the overcast day (IOP 4, Figure 8b) demonstrated that the spatial resolution of these satellite images was not enough to properly describe the heterogeneity of the LST in the UIB Campus.

IV. Effects of the Advection in the surface energy budget at different scales

The surface energy budget is intended to take into account all the energy exchanges taking place in a volume across the atmosphere-surface interface. As indicated in [25], it can be formally derived from the equation of the evolution of the air temperature. In this framework, the four main traditional terms (Rn, H, LE and G) would only balance if no other thermal sources or sinks existed, implying no thermal advection and surface homogeneity. Therefore, once the surface heterogeneity occurs [69], thermal advection will take place, and the usual 4-term energy budget will not close anymore. The SEB was reformulated in [25] as:

$$R_n + H + LE + G + Imb = 0 \qquad (5)$$

where the imbalance (Imb) is the sum of the heat storage in the volume, the biological thermal exchanges, the temperature tendency, the thermal advection and any other unaccounted factor (Imb=S+B+TT+A+Ot). The authors found averaged values of the Imb, for a 2-year series in a locally flat heterogeneous terrain, between 10 and 30% depending on the time of the day and of the year, in good accordance with the estimations of [26]. Then, [19] found that the order of magnitude of the advection term was comparable to the imbalance, provided that persistent hectometer-scale heterogeneities were present around the SEB site.

The present study provides an opportunity to estimate the advection term using a homogeneous data source (the TIR on the UAV) and to check how this estimate changes with the scale of the heterogeneities. The use of the LST derived from the UAV to estimate the different terms in the SEB has been recently explored [21] and results showed variability in the turbulent heat fluxes in a heterogeneous region (100 m) but assumed the imbalance as zero.

Figure 10 shows the daily evolution (21/07/2016, IOP5) of the 4 main fluxes plus the imbalance term measured every 30 minutes (5) in the SEB station installed in the UIB Campus (yellow circle in Figure 1). The Imb shows percentages with respect to the Rn+G combined fluxes of approximately 10-20 % between 0000-0600 UTC and between 1800-2400 UTC, which were greater than the percentage values of H and LE. Between 0600-1800, the Imb represents 20-30 % of the combined fluxes, just exceeded by the H term. Thus, the Imb is a very important term to take into account in the studies of energy fluxes exchange, and the causes of this term deserve to be analyzed.

The importance of the advection term (*A*) in the SEB equation, which represents the effect of the motions of timescales longer than the turbulence-averaged ones, was addressed in [19]. This advection term is expressed as:

$$A = \rho C_p \Delta z U \frac{\Delta T}{\Delta x} \quad (6)$$

where ρ is the air density, Cp is the heat capacity at constant pressure, u is the wind speed, ΔT is the thermal gradient between two points and Δx the distance between them, Δz is the measurement height (2 m) of the atmospheric variables. This expression makes an arbitrary choice taking the height of the measurement as 2 m, to be consistent with the box-approach made in [25]. Therefore, the values are just indicative, whereas the changes are more meaningful.

The study [19] analyzed the order of magnitude of the A term, obtained with data from different sources during the BLLAST campaign [61]. Several simplifications were based on a strong hypothesis, such as neglecting the vertical advection or taking the wind speed of 1 m/s as the order of magnitude in the surface layer. It was found that the contribution of the scales greater than a kilometer to the advection term is very small, whereas at the meter scale, it is too large to be meaningful, and its effects are probably already included in the turbulent sensible heat flux. As long as the scales represent persistent motions (therefore non-turbulent), the scales in between a few decameters or some hectometers, may explain a significant part of the imbalance.

In this work, we discuss if the imbalance measured at the SEB station at the UIB Campus for the IOP 5 (21/07/2016) to the advection terms calculated by (6) with the LST product of the UAV-TIR camera at different spatial resolution, after degrading the original resolution of 2 m x 2 m to decameter or hectometer resolutions. In comparison with [19], in this study, the LST variability is taken approximately 4 times larger in the daytime than the temperature at 2 m and is similar in the nighttime, according to (Gemma Simó personal communication). Therefore, the daytime values are overestimated. The $\rho C_p \Delta z u$ term in (6) is calculated with the actual wind speed data, whereas the absolute values of the temperature gradients are computed between each pixel and the four (north, south, east and west) contiguous pixels, taking the mean value of those four gradients. As a supplement, the advection terms retrieved with the LST product of the Landsat 7-ETM+ and ASTER (daytime and nighttime overpass) are also calculated. The signs of the wind speed and of the temperature gradient are ignored, and the corresponding values are upper value estimations.

Figure 11 shows the imbalance measured between 0400 and 2200 UTC of the IOP5 (21/07/2016) in the SEB station. It shows values below 25 W/m^2 at night with an absolute minimum near dusk. As the morning progresses, the imbalance increases to values near 100 W/m^2 during the central part of the day, decreasing gradually during the afternoon. This evolution is very well mimicked by the estimated advection term computed at a resolution of 200 m x 200 m, which captures well the dusk minimum, the morning increase and the afternoon decrease. The value of advection increases with decreasing resolution until 200 m x 200 m, leveling off for lower resolutions. Instead, in the morning, the advection term at 200 m x 200 m is uncorrelated with the imbalance, indicating that other factors could be important.

The advection terms at the decameter scale (represented by the curve at a resolution of 50 m x 50 m) increase in the afternoon compared to the morning and early afternoon. The curve at 2 m x 2 m is very similar to that at 50 m x 50 m; however, it takes much larger values, indicating that the thermal homogeneities at these scales may be handled by turbulence mixing. The values computed from ASTER, which has a resolution of 90 m x 90 m, are similar to the hectometer ones, whereas those from Landsat 7 ETM+ (at 30 m x 30 m) are larger, similar to what occurs with the corresponding degraded resolution of the UAV-TIR Camera product.

Consequently, we see that the estimated value of the advection term increases with the resolution at which it is computed and that the hectometer scales are the ones that behave qualitatively and quantitatively more similar to the imbalance of the surface energy budget, at least for a cloudless day. For an overcast case, the advection estimate would be smaller due to the low LST heterogeneities observed during the day (IOP4, Figure 9). The underestimation in the morning may be related to other intervening factors, for instance, an underestimation of the latent heat flux, confirming the conclusions reached in [19], and making more realistic advection calculations than those made in that work. However, the advection term cannot close the SEB equation (5) since it is obvious that there exist other terms that should also be taken into consideration.

V. Conclusions

A heterogeneous area containing different types of surfaces located in the University of Balearic Islands in Mallorca (Spain) was the target for an analysis of temperature gradients at high spatial resolutions since recent review studies have reported that land surface temperature heterogeneities within decameter and hectometer scales are not represented in the effective temperature of a kilometric heterogeneous area. New high-resolution orbiting TIR sensors are planned to be launched in the near future, and more studies need to be conducted prior to establishing application methods with such new LST products. On the other hand, a potentially optimum technology, not sufficiently exploited, is the use of an unmanned aerial vehicle carrying a TIR camera onboard. The present study combines both objectives together with the use of the currently orbiting TIR sensors ETM+ and ASTER.

The results show that such LST products, after validation, are capable of detecting significant temperature gradients in a heterogeneous area, which can reach differences, in the case of the UAV-TIR camera system, of up to 18 °C during the morning and 14 °C at night. These differences remain significant with the high-resolution satellite TIR sensors but were not seen with the medium-resolution LST product of the MODIS sensor. An application study of the LST heterogeneity effect on the horizontal imbalance registered in a surface energy balance station was also carried out by means of the estimation of an advection term that takes into account the turbulent heat fluxes produced due to temperature differences between a specific point and the surrounding pixels. The results confirmed that the LST gradients within hectometer resolutions could partly explain the imbalance measured through the advection fluxes; however, the finer scales (decametric or lower resolutions) are too high, indicating that these scales are most likely handled by the turbulent mixing.

From this study, it can be concluded that for heterogeneous zones, LST products from sensors of Landsat series or ASTER are suitable to stipulate the advection term, reducing if it is taken into account, but not fully explaining, the imbalance produced in the SEB budget. This study also opens the application possibilities for decametric LST products of TIR sensors, such as the near-future missions HyspIRI [62], MISTIGRI [63] and THIRSTY [64]. However, further refinements need to be made to retrieve the actual value of the advection term and its influence in the imbalance, from both the in situ and the satellite measurements. However, refinements in this matter need to be made in future works.

The results from the present study are applicable to other zones of the Earth since high-to-medium spatial resolution (~100 m) sensors can be used to estimate the advection contribution to the SEB, as well as to characterize the LST heterogeneity at sub-kilometer scales.

Finally, the potential advantages of using a UAV in this study are worth noting since a better understanding of the LST heterogeneities produced in our area, as well as the possibility of retrieving an LST map under cloudy conditions, was plausible only with the UAV flights.

Acknowledgment

Antoni Mestres and Belen Martí are acknowledged for their help in the field work. The Landsat 7 ETM+ and Terra MODIS images were freely downloaded from the websites glovis.usgs.gov and reverb.echo.nasa.gov, respectively. The ASTER LST& ε products were retrieved from the online websites glovis.usgs.gov, courtesy of the NASA EOSDIS Land Processes Distributed Active Archive Center (LP DAAC), USGS/Earth Resources Observation and Science (EROS) Center, Sioux Falls, South Dakota.

References

[1] M. D. King, "EOS Science Plan: The state of science in the EOS program," Washington, D. C.: NASA, 397, 1999.

[2] J. Li, E. Weisz, and, D.K. Zhou, "Physical retrieval of surface emissivity spectrum from hyperspectral infrared radiances," Geophysical Research Letters, vol. 34, L16812, 2007.

[3] J.M. Sánchez, G. Scavone, V. Caselles, E. Valor, V.A. Copertino, and V. Telesca, "Monitoring daily evapotranspiration at a regional scale from Landsat-TM and ETM+ data: Application to the Basilicata region," Journal of Hydrology, vol. 351, pp. 58–70, 2008.

[4] J. Qin, S. Liang, X. Li and, J. Wang, "Development of the adjoint model of a canopy radiative transfer model for sensitivity study and inversion of leaf area index," IEEE Transactions on Geoscience and Remote Sensing, vol. 46, pp. 2028–2037, 2008.

[5] Z.L. Li, B.H. Tang, H. Wu, H. Ren, G. Yan, et al., "Satellite-derived land surface temperature: Current status and perspectives," Remote Sensing of Environment, vol. 131, pp. 14–37, 2013. http://dx.doi.org/10.1016/j.rse.2012.12.008.

[6] C. Coll, V. García-Santos, R. Niclòs, and, V. Caselles, "Test of the MODIS Land Surface Temperature and emissivity separation algorithm with ground measurements over a rice paddy," IEEE Trans. Geosci. Remote Sens., vol. 54, pp. 3061–3069, 2016.

[7] R. Niclòs, et al., "SMOS-MIRAS level 2 soil moisture product validation in croplands of the Pampean region of Argentina," IEEE Trans. Geosci. Remote Sens., vol. 54, no. 1, pp. 499–512, 2016.

[8] W. Yu and, M. Ma, "Scale mismatch between in situ and remote sensing observations of Land Surface Temperature: Implications for the validation of remote sensing LST products," IEEE Geosci. Remote Sens. Lett., vol. 12, pp. 497–501, 2015.

[9] M. Maimaitiyiming, A. Ghulam, T. Tiyip, F. Pla, P. Latorre-Carmona, et al., "Effects of green space spatial pattern on land surface temperature: Implications for sustainable urban planning and climate change adaptation," ISPRS Journal of Photogrammetry and Remote Sensing, vol. 89, pp. 59-66, (2014). http://dx.doi.org/10.1016/j.isprsjprs.2013.12.010.

[10] H.C. Ho, A. Knudby, P. Sirovyak, Y. Xu, M. Hodul and, S.B. Henderson, Mapping maximum urban air temperature on hot summer days, Remote Sensing of Environment, 154, 38-45, 2014. http://dx.doi.org/10.1016/j.rse.2014.08.012.

[11] M. Abuzar, A. McAllister and, D. Whitfield, "Mapping Irrigated Farmlands Using Vegetation and Thermal Thresholds Derived from Landsat and ASTER Data in an Irrigation District of Australia," Photogrammetric Engineering & Remote Sensing, vol. 81, no. 3, pp. 229-238, 2015. http://dx.doi.org/10.14358/PERS.81.3.229.

[12] P. Fu and, Q. Weng, "Temporal Dynamics of Land Surface Temperature From Landsat TIR Time Series Images," IEEE Geoscience and Remote Sensing Letters, vol. 12, no. 10, pp. 2175-2179, 2015. Doi: 10.1109/LGRS.2015.2455019.

[13] C. Quintano, A. Fernández-Manso, L. Calvo, E. Marcos and, L. Valbuena, "Land surface temperature as potential indicator of burn severity in forest Mediterranean ecosystems," International Journal of Applied Earth Observation and Geoinformation, vol. 36, pp. 1-12, 2015. http://dx.doi.org/10.1016/j.jag.2014.10.015.

[14] A.N. French, D.J. Hunsaker and, K.R. Thorp, "Remote sensing of evapotranspiration over cotton using the TSEB and METRIC energy balance models," Remote Sensing of Environment, vol. 158, pp. 281-294, 2015. http://dx.doi.org/10.1016/j.rse.2014.11.003.

[15] M. Mira, A. Olioso, B. Gallego-Elvira, D. Courault, S. Garrigues, et al., "Uncertainty assessment of surface net radiation derived from Landsat images," Remote Sensing of Environment, vol. 175, pp. 251-270, 2016. http://dx.doi.org/10.1016/j.rse.2015.12.054.

[16] S.P. Grigsby, G.C. Hulley, D.A. Roberts, C. Scheele, S.L. Ustin and, M.M. Alsina, "Improved surface temperature estimates with MASTER/AVIRIS sensor fusion," Remote Sensing of Environment, vol. 167, pp. 53-63, 2015. http://dx.doi.org/10.1016/j.rse.2015.05.019.

[17] A.R. Cummings, A. McKee, K. Kulkarni and, N. Markandey, "The Rise of UAVs," Photogrammetric Engineering & Remote Sensing, vol. 83, no. 4, pp. 317-325, 2017. https://doi.org/10.14358/PERS.83.4.317.

[18] Editors IJRS, "Unmanned aerial vehicles for environmental applications," International Journal of Remote Sensing, vol. 38, no. 8-10, pp. 2029-2036, 2017. DOI: 10.1080/01431161.2017.1301705.

[19] J. Cuxart, B. Wrenger, D. Martínez-Villagrasa, J. Reuder, M.O. Jonassen, et al., "Estimation of the advection effects induced by surface heterogeneities in the surface energy budget," Atmos. Chem. Phys., vol. 16, pp. 9489-9504, 2016. https://doi.org/10.5194/acp-16-9489-2016.

[20] B. Wrenger and, J. Cuxart, "Evening Transition by a River Sampled Using a Remotely-Piloted Multicopter," Boundary-Layer Meteorol., vol. 165, no. 3, pp. 535–543, 2017. https://doi.org/10.1007/s10546-017-0291-9.

[21] C. Brenner, C.E. Thiem, H.-D. Wizemann, M. Bernhardt and, K. Schulz, "Estimating spatially distributed turbulent heat fluxes from high-resolution thermal imagery acquired with a UAV system," International Journal of Remote Sensing, vol. 38, pp. 8-10, 2017.

[22] A. Nishar, S. Richards, D. Breen, J. Robertson and, B. Breen, "Thermal infrared imaging of geothermal environments and by an unmanned aerial vehicle (UAV): A case study of the Wairakei – Tauhara geothermal field, Taupo, New Zealand," Renewable Energy, vol. 86, pp. 1256-1264, 2016. http://dx.doi.org/10.1016/j.renene.2015.09.042.

[23] S.N. Longmore, R.P. Collins, S. Pfeifer, S.E. Fox, M. Mulero-Pázmány, et al., "Adapting astronomical source detection software to help detect animals in thermal images obtained by unmanned aerial systems," International Journal of Remote Sensing, vol. 38, pp. 8-10, 2017.

[24] C. Torresan, A. Berton, F. Carotenuto, S.F. De Gennaro, B. Gioli, et al., "Forestry Applications of UAVs in Europe: A Review." International Journal of Remote Sensing, vol. 38, pp. 2427–2447, 2017. doi:10.1080/01431161.2016.1252477.

[25] J. Cuxart, L. Conangla and, M.A. Jiménez, “Evaluation of the surface energy budget equation with experimental data and the ECMWF model in the Ebro Valley,” J Geophys Res Atmos, vol. 120, no. 3, pp. 1008–1022, 2015.

[26] T. Foken, “The energy balance closure problem: an overview,” Ecological Applications, vol. 18, no. 6, pp. 1351-1367, 2008.

[27] G. Simó, V. García-Santos, M.A. Jiménez, D. Martínez-Villagrasa, R. Picos, et al., “Landsat and Local Land Surface Temperatures in a Heterogeneous Terrain Compared to MODIS Values,” Remote Sens., vol. 8, pp.849, 2016.

[28] G. Simó, D. Martínez-Villagrasa, M. A. Jiménez, V. Caselles and, J. Cuxart, “Impact of the Surface-Atmosphere Variables on the relation between Air and Surface Temperatures,” Pure and Applied Geophysics, 2017. (In press).

[29] J. Cuxart, M.A. Jiménez and, D. Martínez, “Nocturnal Meso-Beta Basin and Katabatic Flows on a Midlatitude Island,” Mon. Wea. Rev., vol. 135, pp. 918–932, 2007. https://doi.org/10.1175/MWR3329.1.

[30] J. Cuxart, M. A. Jiménez, M. Telišman Prtenjak, and, B. Grisogono, “Study of a sea-breeze case through momentum, temperature, and turbulence budgets,” Journal of Applied Meteorology and Climatology, vol. 53, no. 11, pp. 2589-2609, 2014.

[31] M.A. Jiménez, G. Simó, B. Wrenger, M. Telisman-Prtenjak, J.A. Guijarro and, J. Cuxart, “Morning transition case between the land and the sea breeze regimes,” Atmospheric Research, vol. 172, pp. 95-108, 2016. http://dx.doi.org/10.1016/j.atmosres.2015.12.019.

[32] A. Aubinet, T. Vesala and, D. Papale, “Eddy Covariance: A Practical Guide to Measurement and Data Analysis,” Springer Atmospheric Sciences, Springer Verlag, pp. 438, 2012.

[33] D. Martínez-Villagrasa, M. Lehner, C.D. Whiteman, S.W. Hoch and, J. Cuxart, “The upslope–downslope flow transition on a basin sidewall,” J. Appl. Meteor. Climatol., vol. 52, pp. 2715–2734, 2013. doi:https://doi.org/10.1175/JAMC-D-13-049.1.

[34] C. Liebethal, B. Huwe and, T. Foken, “Sensitivity analysis for two ground heat flux calculation approaches,” Agric. Forest. Meteorol., vol. 132, no. 3, pp. 253–262, 2005.

[35] W.C. Snyder, Z. Wan, Y. Zhang and, Y.Z. Feng, “Classification-based emissivity for Land Surface Temperature measurement from space,” Remote Sens., vol. 19, pp. 2753–2774, 1998.

[36] W. Brutsaert, “On a derivable formula for long-wave radiation from clear skies,” Water Resour. Res., vol. 11, no. 5, pp. 742–744, 1975. doi:10.1029/WR011i005p00742.

[37] E. Theocharous and, N.P. Fox, “CEOS comparison of IR brightness temperature measurements in support of satellite validation. Part II: Laboratory comparison of the brightness temperature of blackbodies,” NPL Rep. OP4, Natl. Phys. Lab., Teddington, U. K, 2010.

[38] Z. Wan and, J. Dozier, “A generalized split-window algorithm for retrieving land-surface temperature from space,” IEEE Transactions on Geoscience and Remote Sensing, vol. 34, no. 4, pp. 892-905, 1996. doi: 10.1109/36.508406.

[39] Z. Wan, “New refinements and validation of the collection-6 MODIS land-surface temperature/emissivity product,” Remote Sensing of Environment, vol. 140, pp. 36-45, 2014. http://dx.doi.org/10.1016/j.rse.2013.08.027.

[40] Y. Yamaguchi, A.B. Kahle, H. Tsu, T. Kawakami and, M. Pniel, “Overview of advanced spaceborne thermal emission and reflection radiometer (ASTER),” IEEE Trans. Geosci. Remote Sens., vol. 36, pp. 1062–1071, 1998.

[41] A. Gillespie, S. Rokugawa, T. Matsunaga, C.J. Cothern, S. Hook and, A.B. Kahle, “A temperature and emissivity separation algorithm for Advanced Spaceborne Thermal Emission and Reflection Radiometer (ASTER) images,” IEEE Trans. Geosci. Remote Sens., vol. 36, pp. 1113–1126, 1998.

[42] C. Coll, V. Caselles, E. Valor, R. Niclos, J.M. Sánchez, et al. , “Temperature and emissivity separation from ASTER data for low spectral contrast surfaces,” Remote Sensing of Environment, vol. 110, pp. 162-175, 2007.

[43] H. Tonooka, “Accurate atmospheric correction of ASTER thermal infrared imagery using the WVS method,” IEEE Transactions on Geoscience and Remote Sensing, vol. 43, pp. 2778–2792, 2005.

[44] N. Malakar and, G.C. Hulley, “A Water Vapor Scaling Model for Improved Land Surface Temperature and Emissivity Separation of MODIS Thermal Infrared Data,” Remote Sensing of Environment, vol. 182, pp. 252-264, 2016. DOI: 10.1016/j.rse.2016.04.023.

[45] Landsat 7 Science Data Users Handbook, “Technical Report, U.S. Geological Survey,” Available online: http://landsathandbook.gsfc.nasa.gov (accessed on 1 August 2016), 1998.

[46] S.J. Hook, A.R. Gabell, A.A. Green and, P.S. Kealy, “A comparison of techniques for extracting emissivity information from thermal infrared data for geologic studies,” Remote Sens. Environ., vol. 42, pp. 123–135, 1992.

[47] G.C. Hulley, S.J. Hook, E. Abbott, N. Malakar, T. Islam and, M. Abrams, “The ASTER Global Emissivity Dataset (ASTER GED): Mapping Earth’s emissivity at 100 m spatial scale,” Geophys. Res. Lett., vol. 42, pp. 7966–7976, 2015.

[48] A. Berk, G.P. Anderson, P.K. Acharya, L.S. Bernstein, L. Muratov, et al., “MODTRAN5: 2006 update,” Proc. SPIE, 2006. doi:10.1117/12.665077.

[49] J.A. Barsi, J.R. Schott, F.D. Palluconi and, S.J. Hook, “Validation of a web-based atmospheric correction tool for single thermal band instruments,” Proc. SPIE, 2005. doi:10.1117/12.619990.

[50] E. Kalnay, M. Kanamitsu, R. Kistler, W. Collins, D. Deaven, et al., “NCEP/NCAR 40 year reanalysis project,” Bull. Amer. Meteor. Soc., vol. 77, no. 3, pp. 437–471, 1996.

[51] L. Pérez-Planells, V. García-Santos and, V. Caselles, “Comparing different profiles to characterize the atmosphere for three MODIS TIR bands,” Atmos. Res., vol. 161–162, pp. 108–115, 2015.

[52] FLIR LEPTON Datasheet, “Document Number: 500-0763-01-09 Rev 110,” Available online: http://www.flir.com (accessed on 17 July 2017), 2015.

[53] J. Cheng, S. Liang, Y. Yao and, X. Zhang, “Estimating the Optimal Broadband Emissivity Spectral Range for Calculating Surface Longwave Net Radiation,” IEEE Geoscience and Remote Sensing Letters, vol. 10, no. 2, pp. 401-405, 2013. doi: 10.1109/LGRS.2012.2206367.

[54] C. Coll, V. Caselles, J.M. Galve, E. Valor, R. Niclòs, et al., “Ground measurements for the validation of land surface temperatures derived from AATSR and MODIS data,” Remote Sensing of Environment, vol. 97, pp. 288−300, 2005.

[55] H. Tonooka and, F.D. Palluconi, “Validation of ASTER/TIR standard atmospheric correction using water surfaces,” IEEE Trans. Geosci. Remote Sens., vol. 43, pp. 2769–2777, 2005. doi:10.1109/TGRS.2005.857883.

[56] S.J. Hook, R.G. Vaughan and, H. Tonooka, “Absolute radiometric inflight validation of mid infrared and thermal infrared data from ASTER and MODIS on the Terra spacecraft using the Lake Tahoe CA/NV, USA, Automated Validation Site,” IEEE Trans. Geosci. Remote Sens., vol. 45, pp. 1798–1807, 2007.

[57] C. Coll, J.M. Galve, J.M. Sánchez and, V. Caselles, “Validation of Landsat-7/ETM+ thermal-band calibration and atmospheric correction with ground-based measurements,” IEEE Transa. Geosci. Remote Sens., vol. 48, pp. 547–555, 2010.

[58] F. Li, T.J. Jackson, W.P. Kustas, T.J. Schmugge, A.N. French, et al., “Deriving Land Surface Temperature from Landsat 5 and 7 during SMEX02/SMACEX,” Remote Sens. Environ., vol. 92, pp. 521–534, 2004.

[59] M.A. Jiménez and, J. Cuxart, “Study of the probability density functions from a large-eddy simulation for a stably stratified boundary layer,” Bound Layer Meteorol., vol. 118, pp. 401–420, 2006.

[60] H. Tennekes and, J. L. Lumley, “A First Course in Turbulence,” The Massachusetts Institute of Technology, pp. 300, 1982.

[61] M. Lothon, et al., “The BLLAST field experiment: Boundary-Layer Late Afternoon and Sunset Turbulence,” Atmos. Chem. Phys., vol. 14, pp. 10931-10960, 2014. https://doi.org/10.5194/acp-14-10931-2014.

[62] D.A. Roberts, D.A. Quattrochi, G.C. Hulley, S.J. Hook and, R.O. Green, “Synergies between VSWIR and TIR data for the urban environment: An evaluation of the potential for the Hyperspectral InfraredImager (HyspIRI) Decadal Survey mission,” Remote Sens. Environ., vol. 117, pp. 83–101, 2012. doi:10.1016/j.rse.2011.07.021.

[63] J.P. Lagouarde, M. Bach, J.A. Sobrino, G. Boulet, X. Briottet, et al., “The MISTIGRI thermal infrared project: Scientific objectives and mission specifications,” International Journal of Remote Sensing, vol. 34 , no. 9, pp. 3437-3466, 2013. http://dx.doi.org/10.1080/01431161.2012.716921.

[64] S. Hook, J.P. Lagouarde, P. Crébassol, B. Boissin, P. Gamet, et al., “THIRSTY — A new thermal infrared mission concept for Earth science,” 4th international symposium on recent advances in quantitative remote sensing RAQRS'IV, Valencia, Spain, 22–26th September 2014.

[65] Smith, J.A. and Ballard, J.R., “Effect of spatial resolution on thermal and near-infrared sensing of canopies.” Optical Engineering, vol. 38, no. 8, pp.1413-1424, 1999.

[66] Lagouarde, Jean-Pierre, Herve Ballans, Patrick Moreau, Dominique Guyon, and Damien Coraboeuf. "Experimental study of brightness surface temperature angular variations of maritime pine (Pinus pinaster) stands." Remote sensing of environment vol. 72, no. 1, 17-34, 2000.

[67] Liu, Qinhuo, Huaguo Huang, Wenhan Qin, Kaihua Fu, and Xiaowen Li. "An extended 3-D radiosity– graphics combined model for studying thermal-emission directionality of crop canopy." IEEE transactions on geoscience and remote sensing, vol. 45, no. 9, pp. 2900-2918, 2007).

[68] V. García-Santos, C. Coll, E. Valor, R. Niclòs, and V. Caselles, “Analyzing the anisotropy of thermal infrared emissivity over arid regions using a new MODIS land surface temperature and emissivity product (MOD21),” Remote Sens. Environ., vol. 169, pp. 212–221, 2015.

[69] Anderson, Martha C., J. M. Norman, John R. Mecikalski, Ryan D. Torn, William P. Kustas, and Jeffrey B. Basara. "A multiscale remote sensing model for disaggregating regional fluxes to micrometeorological scales." Journal of Hydrometeorology 5, no. 2 , pp. 343-363, 2004.

[70] M.A. Jiménez, A. Ruiz, and J. Cuxart, “Estimation of cold pool areas and chilling hours through satellite-derived surface temperatures.” Agricultural and Forest Meteorology, vol. 207, pp. 58-68, 2015. ISSN 0168-1923, https://doi.org/10.1016/j.agrformet.2015.03.017.

[71] Gago, J, Martorell, S, Tomas, M, Pou, A, Millan, B, Ramon, J, Ruiz, M, Sanchez, R, Galmes, J, Conesa, MA, Cuxart, J, Tardaguila, J, Ribas-Carbo, M, Flexas, J, Medrano, H, Escalona, JM. “High-resolution aerial thermal imagery for plant water status assessment in vineyards using a multicopter-RPAS.” In Proceedings of 2013 VII Congreso Ibérico de Agroingeniería y Ciencias Hortícolas, Madrid, Spain, 26–29 August 2013, pp. 1–6.

TABLE LIST

Table I. Date and UTC hour of the daytime and nighttime ASTER sensor passes over the UIB Campus during the period April and November 2016.

	Date	UTC_Hour
Morning ASTER scenes	9-Apr-16	1042
	19-Juny-16	1049
	5-Jul-16	1049
	21-Jul-16	1049
	7-Sep-16	1049
	10-Nov-16	1049
Night ASTER scenes	19-Juny-16	2154
	5-Jul-16	2154
	21-Jul-16	2154
	22-Aug-16	2153
	7-Sep-16	2153

Table II. Date, path/row and UTC hour of the daytime ETM+ sensor passes over the UIB Campus during 2016. Only clear-sky days are considered.

Date	Path/Row	Hour_UTC
20-Jan-16	196/33	1027
28-Feb-16	197/32	1033
9-Apr-16	196/33	1027
16-Apr-16	197/32	1033
2-May-16	197/32	1033
11-May-16	196/33	1027
18-May-16	197/32	1033
19-Jun-16	197/32	1033
28-Jun-16	196/33	1027
5-Jul-16	197/32	1033
21-Jul-16	197/32	1033
30-Jul-16	196/33	1027
15-Aug-16	196/33	1027
16-Sep-16	196/33	1027
23-Sep-16	197/32	1033
9-Oct-16	197/32	1033
3-Nov-16	196/33	1027
10-Nov-16	197/32	1033
28-Dec-16	197/32	1033

Table III. UTC hour of the UAV flights for the 5 IOPs carried out between June and July 2016 at the UIB Campus.

IOP number	Date	UTC Hour										
1	19-Jun-16	0400	0600	0800		1200	1400	1600	1800	2000		
2	28-Jun-16				1000	1200	1400	1600	1800	2000	2200	0230
3	5-Jul-16	0400	0600	0800	1000	1200	1400	1600	1800	2000		
4	14-Jul-16	0400	0600	0800	1000	1200	1400	1600	1800	2000		
5	21-Jul-16	0400	0600	0800	1000	1200	1500		1800	2000	2200	

FIGURES LIST

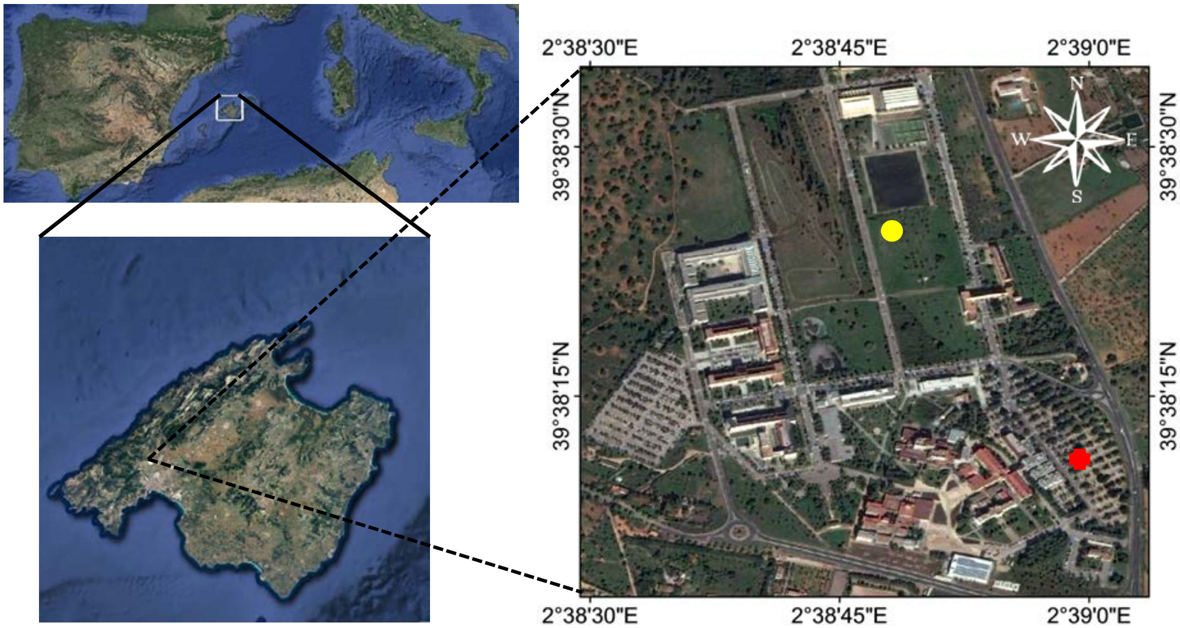

Figure 1. Location of the UIB Campus in Mallorca Island (left) and details of the study area (right), where the different types of surfaces can be observed. The yellow dot indicates the SEB station, while the red cross shows the position where the UAV was launched for all flights. Source: Google Earth.

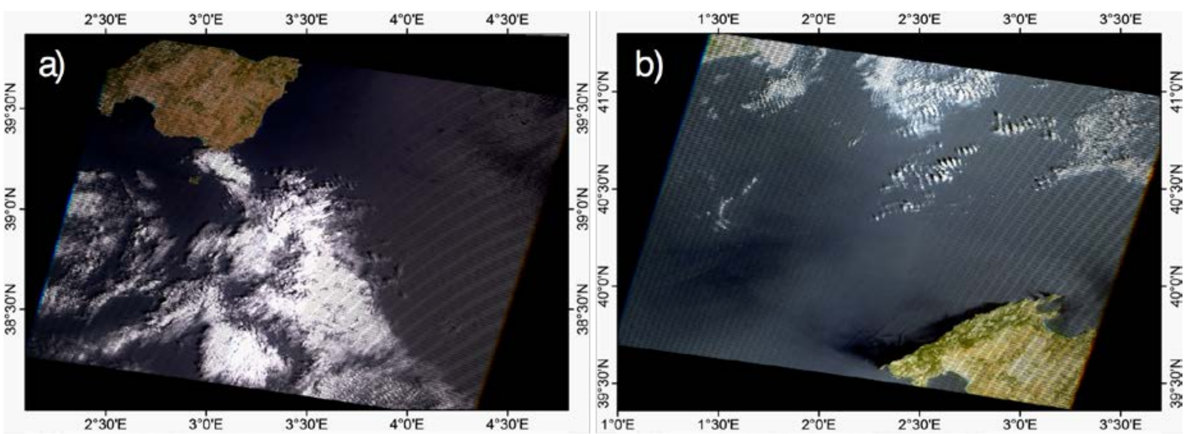

Figure 2. RGB composite of the ETM+ passes over the Mallorca Island in two different orbits: a) path/row 196/33 scene on June 28th of 2016, b) path/row 197/32, July 21st of 2016.

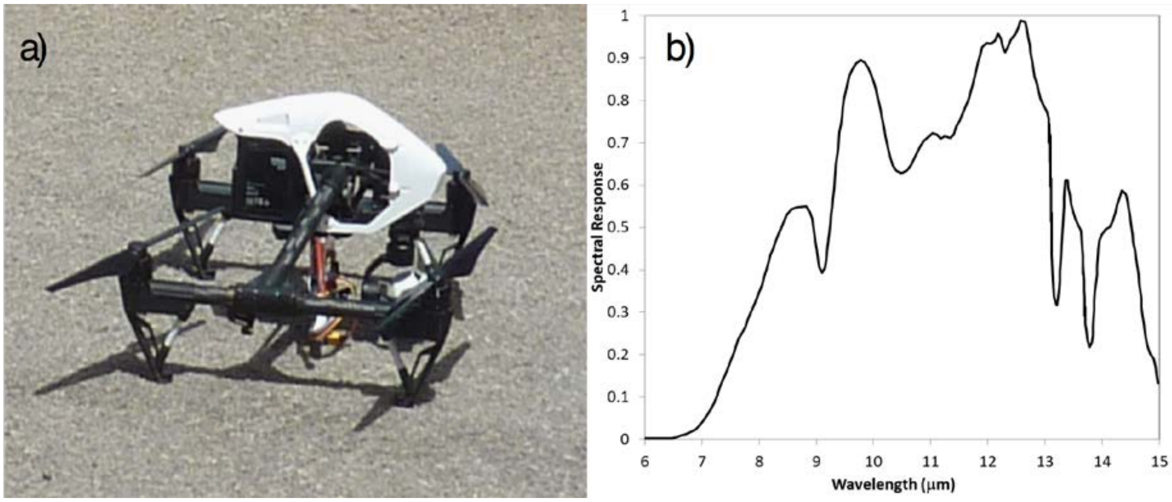

Figure 3. a) Picture of the UAV-TIR camera ensemble prior to start the flight. **b)** Spectral response of the FLIR LEPTON camera in the 6-15-µm range provided by [52].

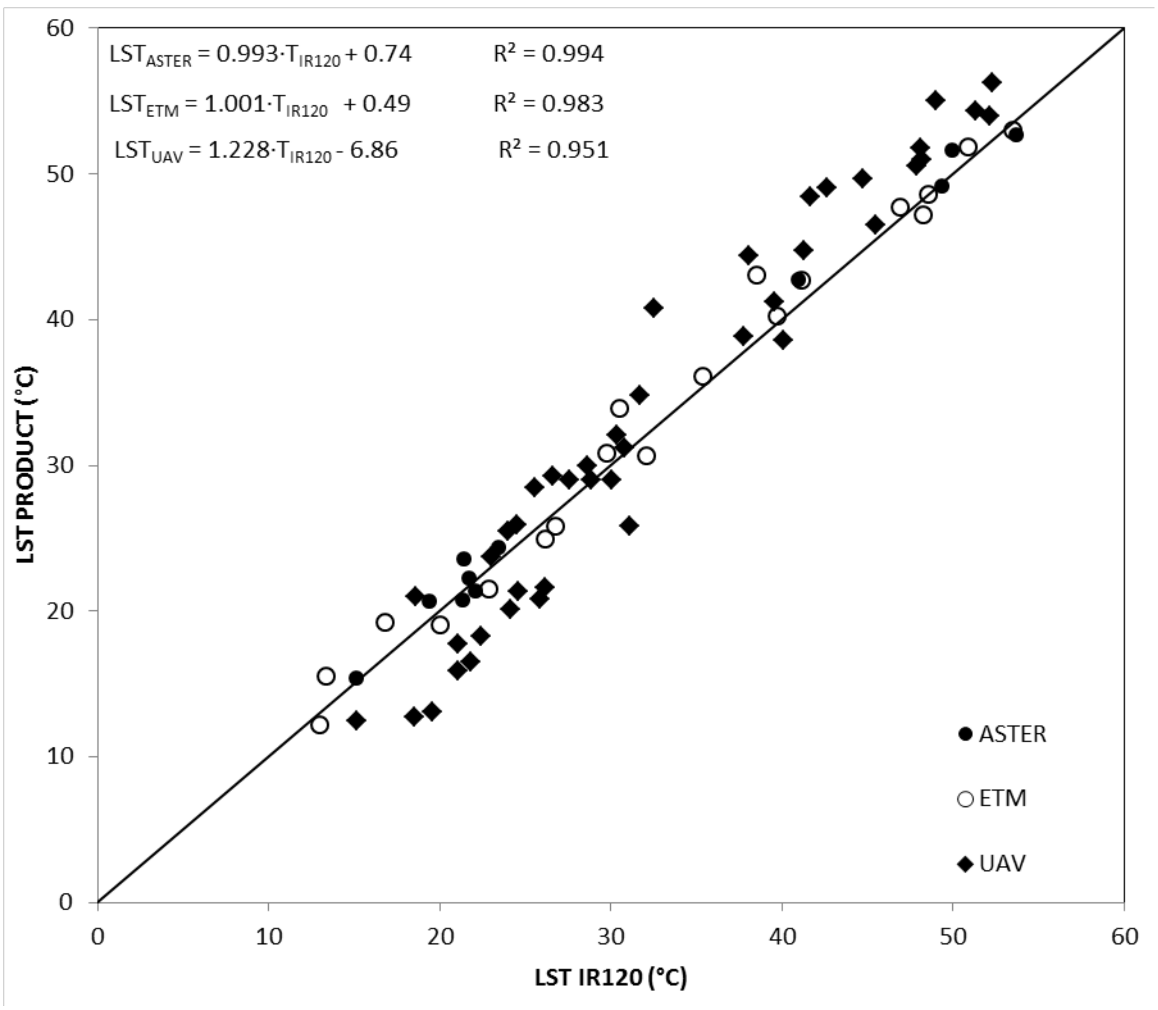

Figure 4. Comparison of the LST measurements of the IR120 field radiometer with LST products retrieved from ASTER (Table 1) and ETM+ (Table 2) orbiting sensors and aerotransported TIR camera (Table 3). Linear trendline for the three sensors and R^2 are included.

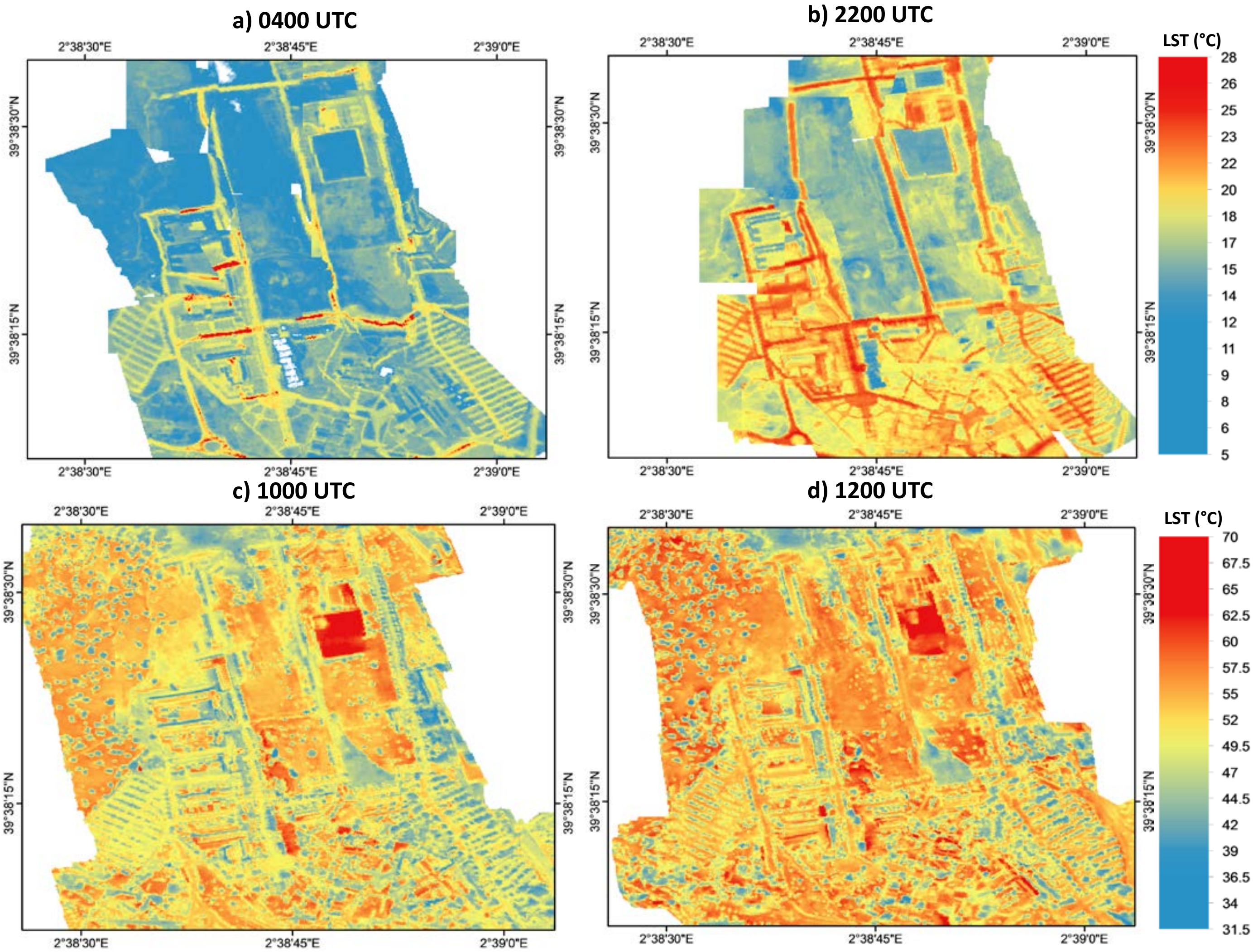

Figure 5. LST maps composed from the scenes registered by the TIR camera assembled in the UAV for the IOP 5 (21/07/2016) for: a) 04:00, b) 22:00, c) 10:00 and d) 12:00 UTC hours.

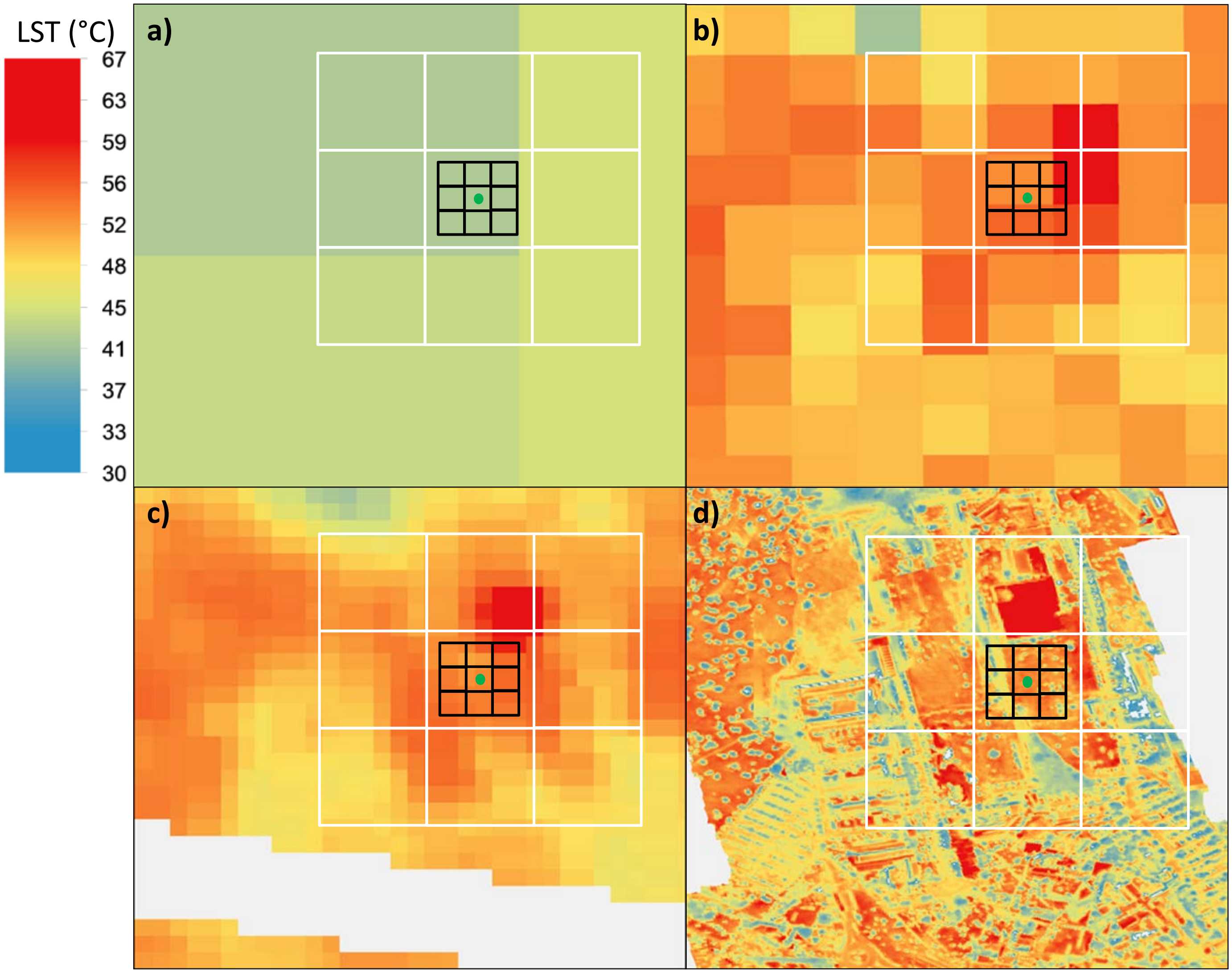

Figure 6. LST products of the simultaneous overpassing sensors on 21/07/2016 (IOP 5) between 1033-1049 UTC for: a) MODIS, b) ASTER, c) ETM+, and d) UAV-TIR camera flight. The SEB station position is shown as a green circle, and the area of pixels used for calculating the spatial gradient for Equation 6 at a 50-m resolution (pixel included in black squares) and 200-m resolution (pixel included in white squares).

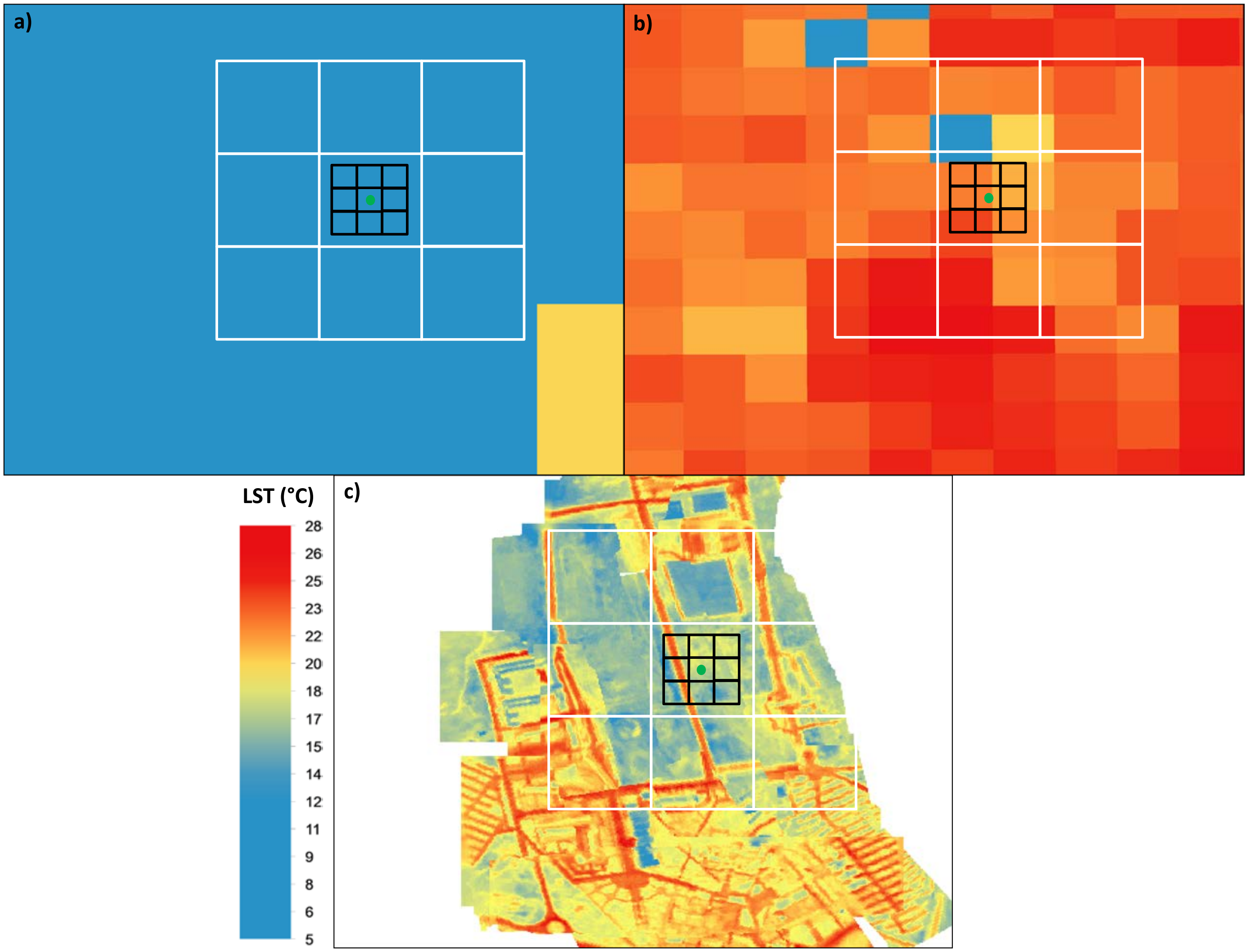

Figure 7. LST products of the simultaneous overpassing sensors on 21/07/2016 (IOP 5) at 2153 UTC for: a) ASTER, b) ETM+, and c) UAV-TIR Camera Flight. SEB station position is shown as the green circle, and the area of pixels used for calculating the spatial gradient for Equation 6 at a 50-m resolution (pixel included in black squares) and 200-m resolution (pixel included in white squares).

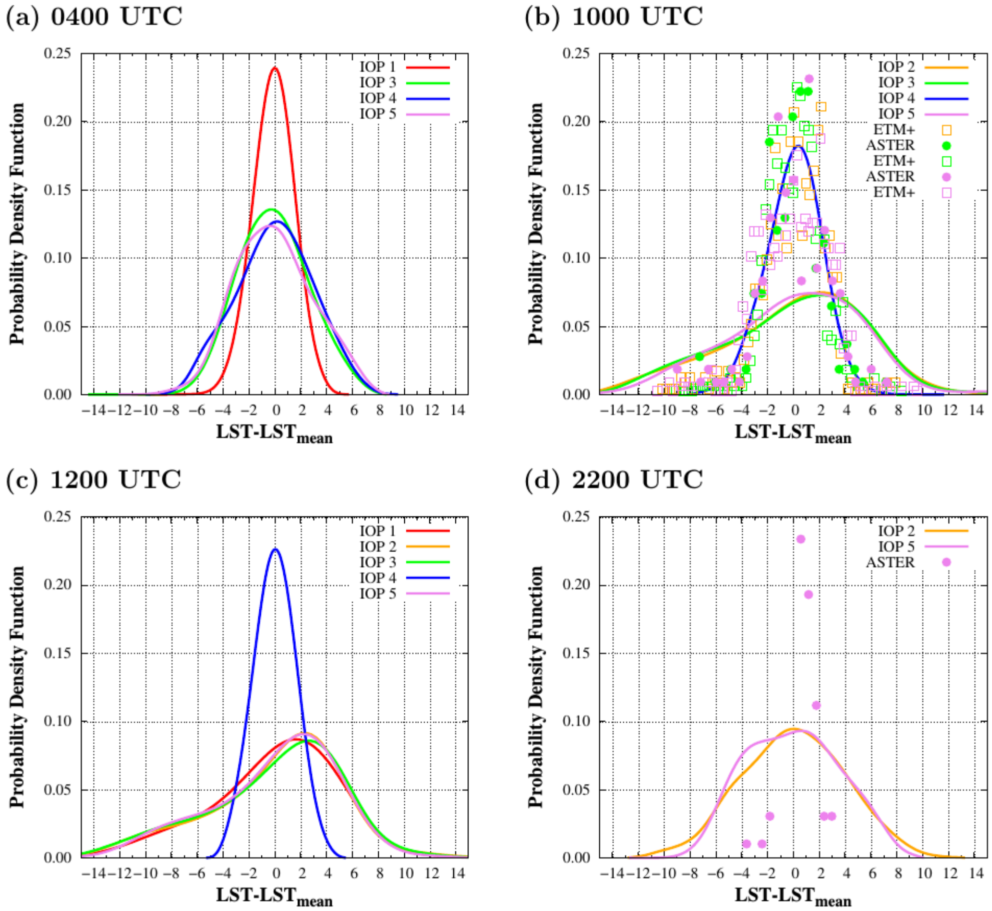

Figure 8. Probability density functions (PDFs) computed from the LST fields over the 1-km square UIB-Campus derived from the multicopter (in lines) and from satellite images (ASTER and ETM+, in points) for several instants: (a) 0400 UTC, (b) 1000 UTC, (c) 1200 UTC, and (d) 2200 UTC. All IOPs are included in the plots. To make the PDFs for all IOPs comparable, the LSTs values in the x-axis are normalized with the corresponding mean value.

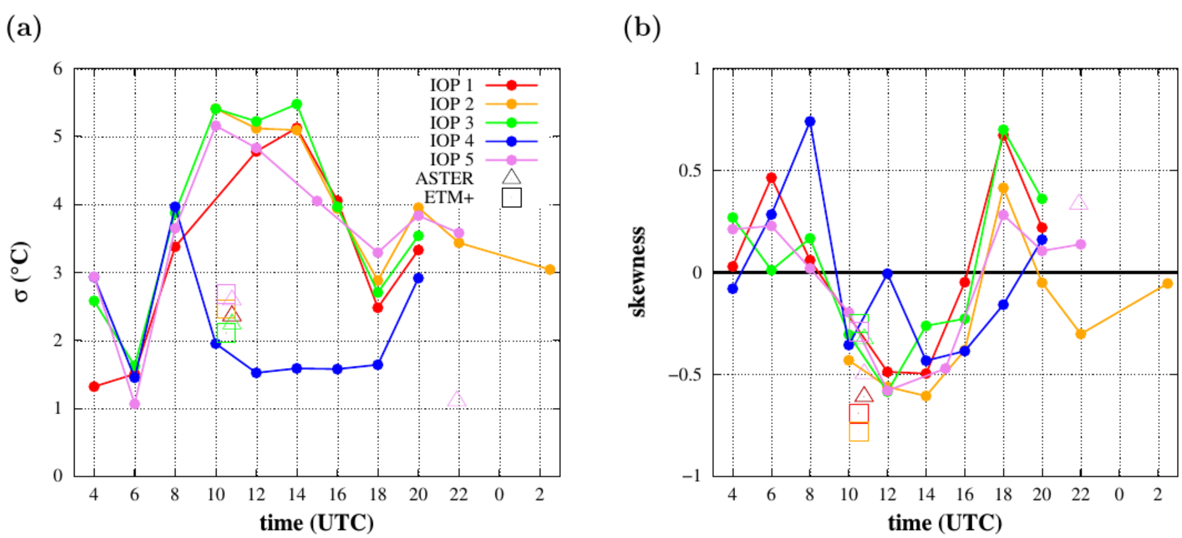

Figure 9. Temporal evolution of the statistical parameters computed from the probability density functions (PDFs) as those in Figure 8 but considering all IOPs: (a) standard deviation and (b) skewness. Those computed from the UAV are shown with circles, whereas the squares and triangles are those computed from ETM+ and ASTER, respectively.

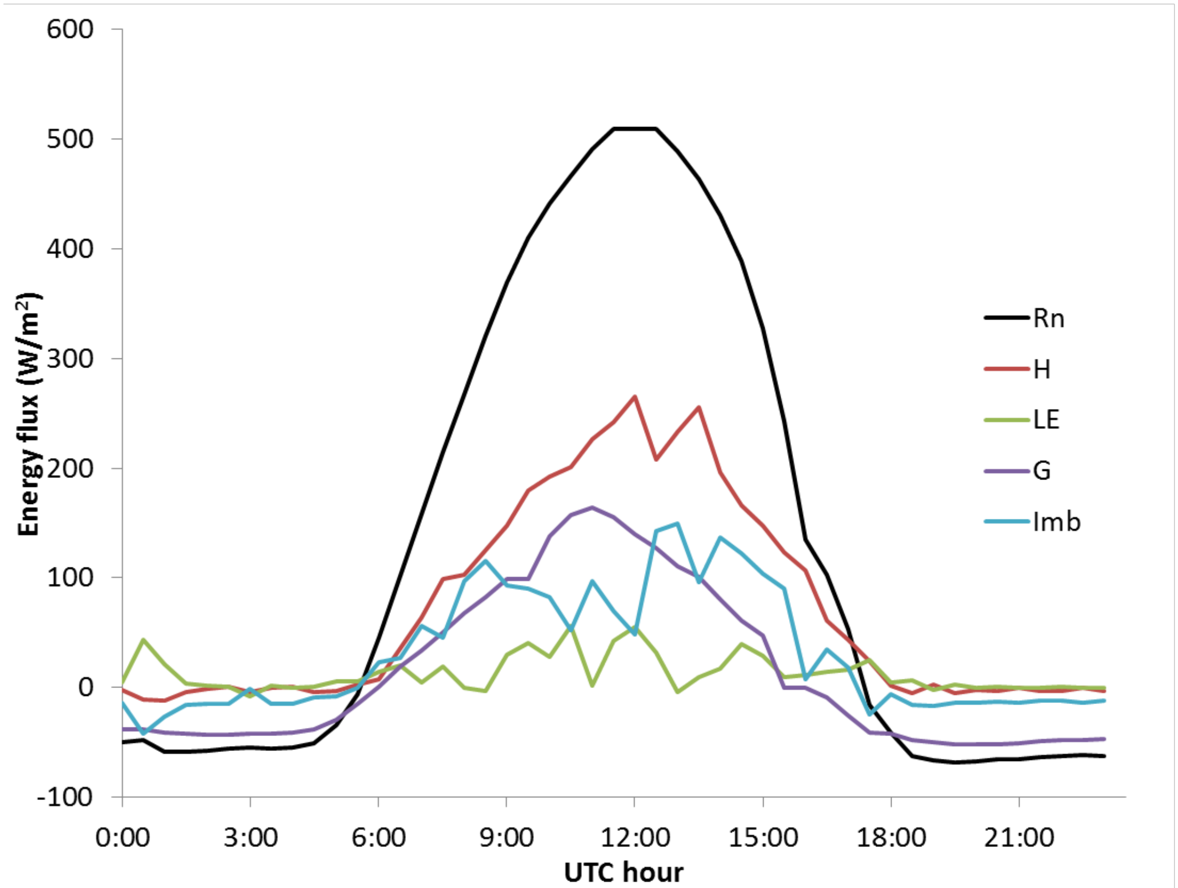

Figure 10. Daily evolution of the four main terms in the SEB equation (Rn, H, G and LE) measured by the SEB station (yellow dot in Figure 1) and the corresponding imbalance (Imb) during 21/07/2016 (IOP 5).

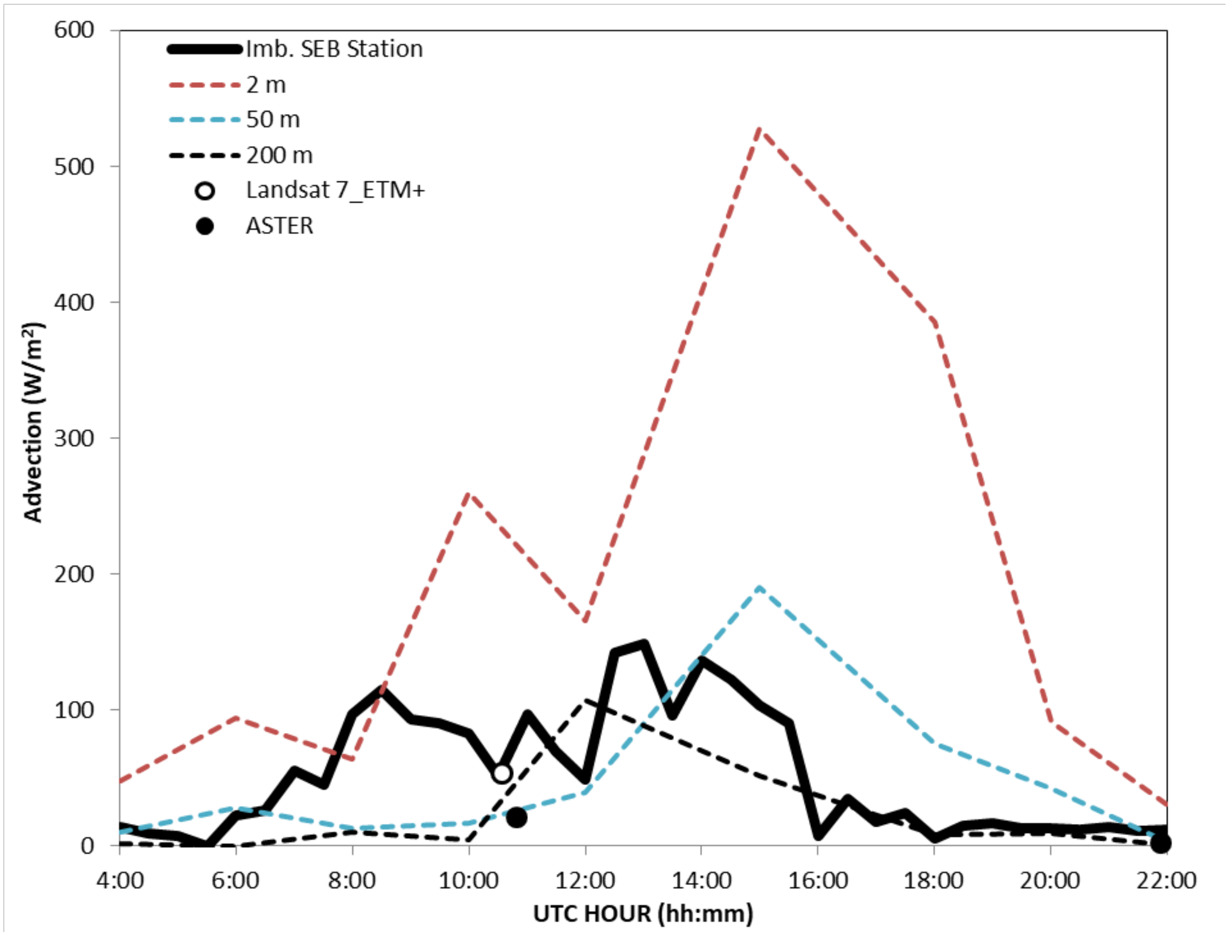

Figure 11. Comparison along different hours of the IOP 5 (21/07/2016) of the imbalance measured in the SEB station with the order of magnitude of the advection term calculated in the same SEB station location with data of the LST map of UAV-TIR camera at the original spatial resolution (2 m x 2 m) and at two different spatial resolutions: a decametric pixel of 50 m x 50 m and a hectometer resolution of 200 m x 200 m, after degrading the original LST map.